Supporting Information

Broadband and large surface enhancements of local electric field enabled by cross-etched hyperbolic metamaterials

Zixian Li[1], Houjiao Zhang[1], Zhonghong Shi[1], Haoyang Li[1], Guoli He[1], Shuang Qiu[1], Zhang-Kai Zhou[1,]*

[1]State Key Laboratory of Optoelectronic Materials and Technologies, School of Physics, Sun Yat-Sen University, Guangzhou 510275, China

Email: *zhouzhk@mail.sysu.edu.cn*

Content

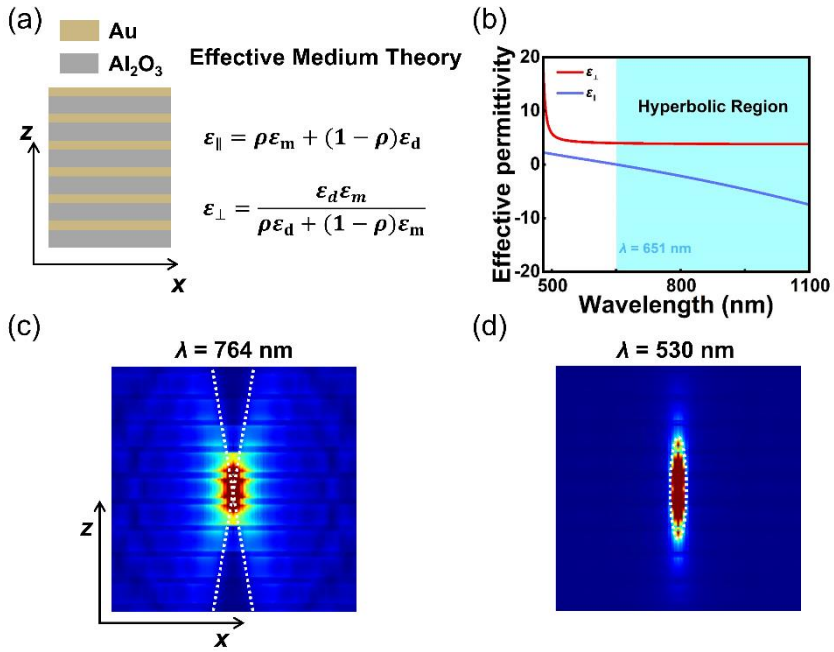

Fig. S1 Permittivity dispersion of multilayer Au/Al_2O_3 HMMs. (a) *xz* profile model and Effective Medium Theory. (b) Hyperbolic dispersion relation of effective permittivity components for multilayer HMMs (ρ = 0.2). (c) The EF distribution of the HMMs excited by a dipole source in its center at λ = 764 nm and (d) λ = 530 nm.

In this paper, the alternating 5 nm Au layer and 20 nm Al_2O_3 layer form the multilayer HMMs, as shown in Fig. S1a. Its effective permittivity components $\varepsilon_{\parallel} = \varepsilon_{xx} = \varepsilon_{yy}$ and $\varepsilon_{\perp} = \varepsilon_{zz}$ can be approximated by Effective Medium Theory (*Nature Photonics*, *7*(12), 948-957), where the ρ representing the volume fraction of the metal, and ε_m and ε_d is the permittivity of the metal (Au) and the dielectric (Al_2O_3), respectively. When the thickness of a metal/dielectric layer is much smaller than the wavelength, the approximate result given by the formula is remarkable.

The multilayer HMMs can achieve opposite signs for $\varepsilon_{\parallel}$ and $\varepsilon_{\perp}$ at λ > 651 nm (Fig. S1b), thus realizing a hyperbolic wavevector Iso-Frequency Contour (IFC). It is meaning that the HMMs can exhibit a unique hyperbolic EF distribution, and can excited by the dipole source placed in HMMs (Fig. S1c and Fig. S1d). It is clear that a hyperbolic wavevector IFC is discernible at λ = 764 nm, whereas at λ = 530 nm, only an elliptical wavevector IFC is detectable. This observation indicates that the multilayer HMMs in this work exhibits hyperbolic characteristics for wavelengths exceeding 651 nm.

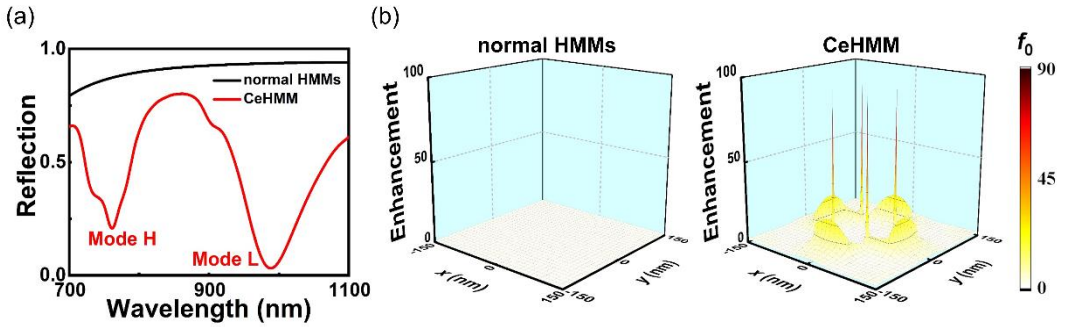

Fig. S2. The comparison of the CeHMMs and normal HMMs. (a) Reflection spectra of CeHMMs (red curve) and normal HMMs (black curve). Compare with the CeHMMs, the normal HMMs exhibit reflection valleys, indicating the failure of sustaining resonant modes under the incident light from free space. (b) The EF enhancement distributions of the CeHMMs (right, f_0 up to 90) and the normal HMMs (left, $f_0 \sim 1.5$) at the incident wavelength of 764 nm. The incident light is left-handed circularly polarized (LCP) in Fig. S2. f_0 is the EF enhancement factor which is defined as $f_0 = |E/E_0|$ (E and E_0 are the EF enhancement under incident light excitation and in free space, respectively).

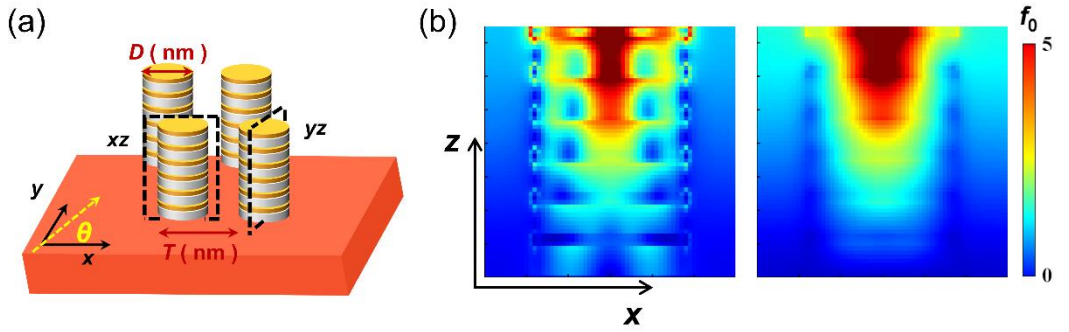

Fig. S3. The EF distributions of nanorod HMMs. (a) Schematic diagram of nanorod HMMs with linearly polarized light incidence (polarization angle θ = 90°). The diameter D = 180 nm, and the period T = 300 nm. (b) The EF enhancement distributions of xz and yz profiles (dashed boxes in Fig. S3a) at λ = 649 nm.

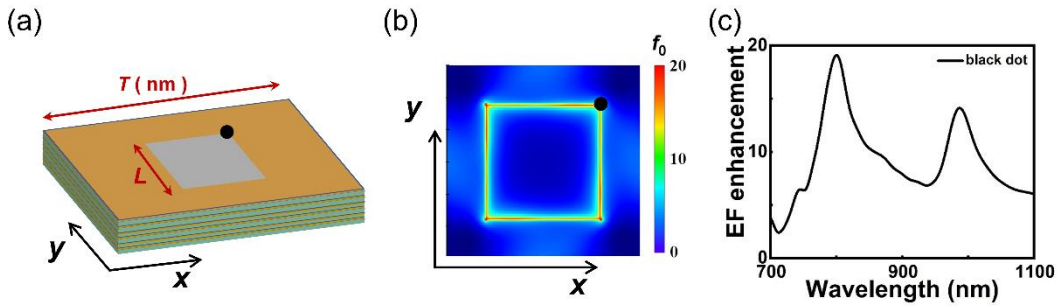

Fig. S4. (a) Schematic of a periodically square-etched HMMs structure under LCP incidence, with the square side length L = 180 nm and the cell period T = 300 nm. (b) The EF enhancement distribution on the top surface, with the black dot indicating the hot spot. (c) The wavelength dependence of EF enhancement at the hot spot.

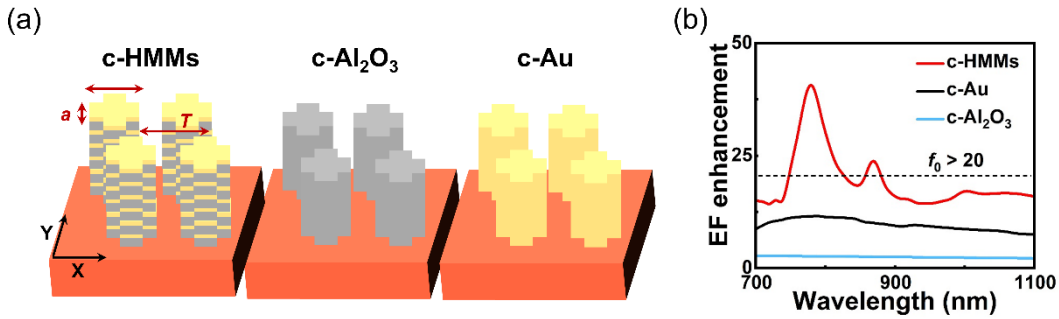

Fig. S5. The wavelength dependence of EF enhancements for the periodic c-HMMs, c-Au and c-Al_2O_3 under LCP incidence (c is the short sign for the cross). (a) Schematic diagram of the cross structure, with the cross-patterned width a = 80 nm, length b = 180 nm and period T = 300 nm. (b) Comparison of spectral ranges (f_0 >20) for these cross structures: c-HMMs (red curve), c-Au (black curve), and c-Al_2O_3 (blue curve).

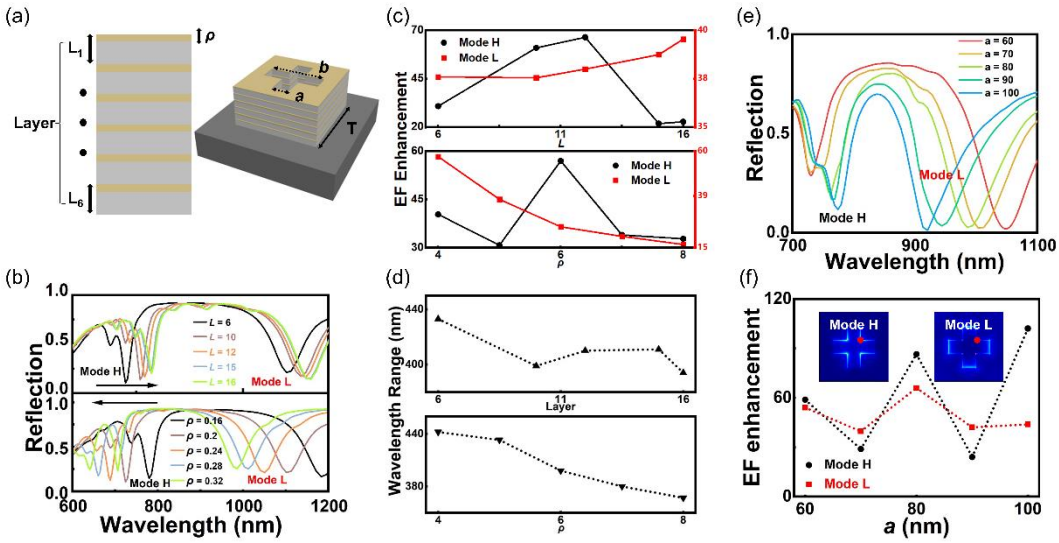

Fig. S6. The influence of the hyperbolic parameters (ρ and L) and cross-shaped width a. (a) The schematic diagram of CeHMMs and its structural parameters. L is the number of metal/dielectric groups, and ρ is the metal volume fraction. The cross-shaped width a, length b, and structural period T are set as 80, 200, and 300 nm, respectively. The total thickness of multilayer CeHMMs is fixed at 150 nm. (b) Reflection spectra for different ρ and L. (c) EF enhancements at hot spots for Mode H (black) and Mode L (red) with varying ρ and L. (d) The spectral range of EF enhancements with f_0 >20 under varied ρ and L. (e) Reflection spectra and (f) EF enhancement at hot spots (red dots within the illustration in Fig. S6d) for Mode H and Mode L with variation in width a, while keeping b = 180 nm and T = 300 nm fixed.

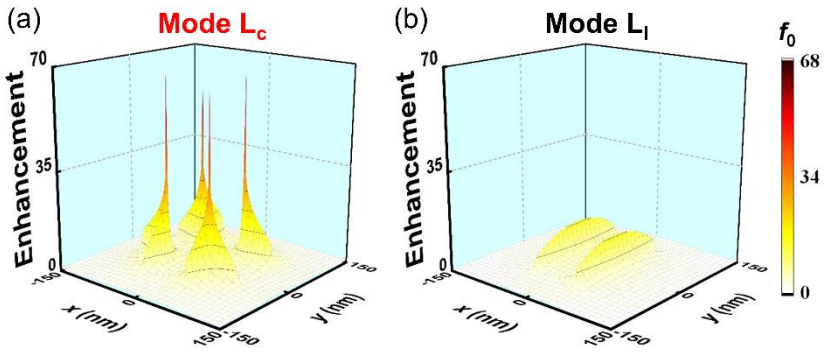

Fig. S7. EF enhancement distributions of Mode L on the surface (z = 0.5 nm) for (a) the CeHMMs and (b) LeHMMs.

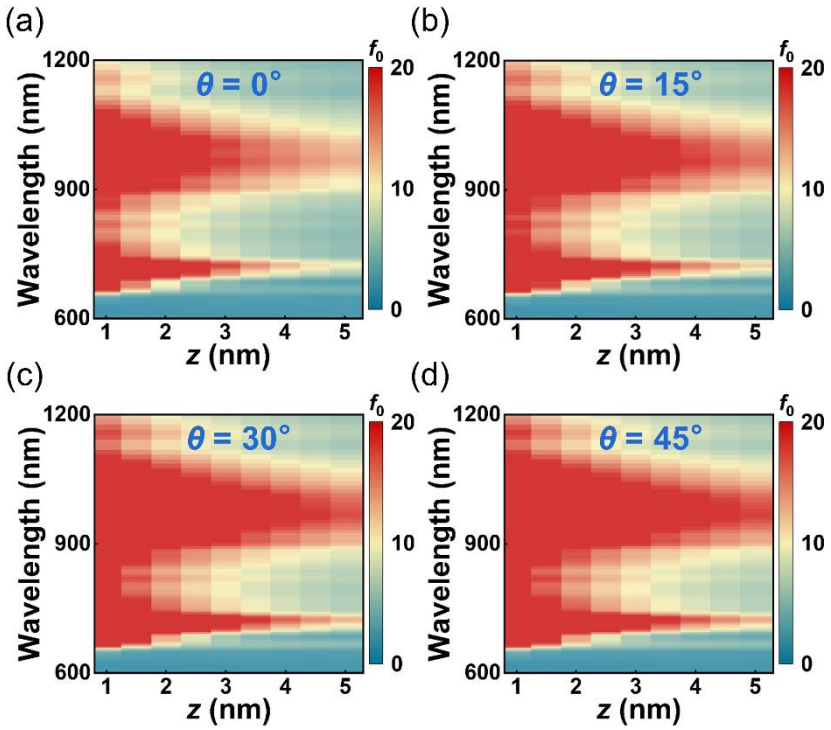

Fig. S8. Two-dimensional (2D) plots of EF enhancements as a function of the wavelength (600~1200 nm) and different xy surface (z ranging from 1 to 5 nm) of the CeHMMs, excited by LPL with different polarization angle (θ): (a) θ = 0°, (b) θ = 15°, (c) θ = 30°, (d) θ = 45°.

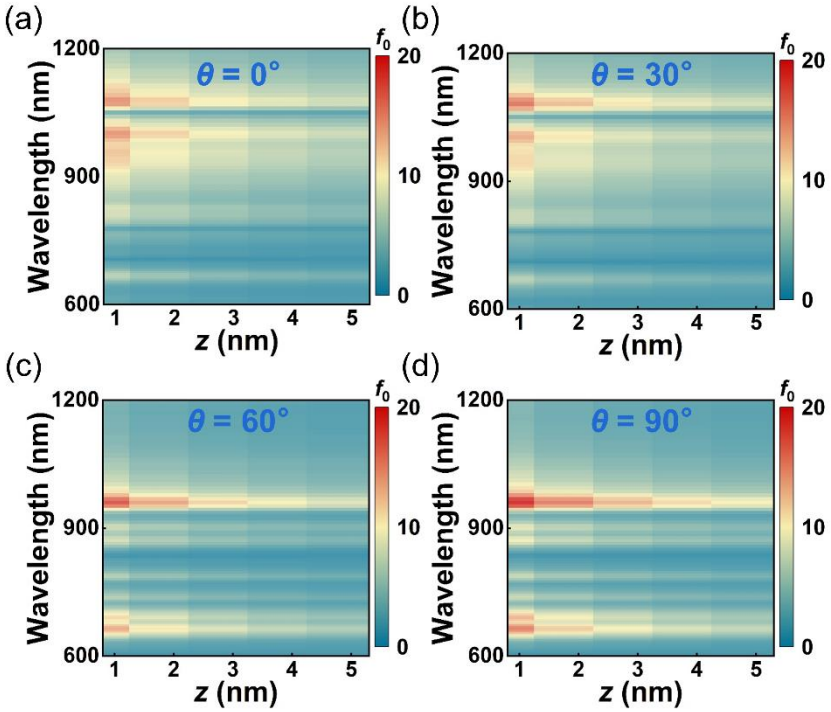

Fig. S9. 2D plots of EF enhancements as a function of the wavelength (600 ~ 1200 nm) and different *xy* surfaces (*z* ranging from 1 to 5 nm) of the LeHMMs, were stimulated by LPL with varying polarization angles (θ): θ = 0°, (b) θ = 30°, (c) θ = 60°, (d) θ = 90°. It is evident that CeHMMs demonstrates the more significant EF enhancement and the broader spectral range (f_0 >20) compared to LeHMMs.

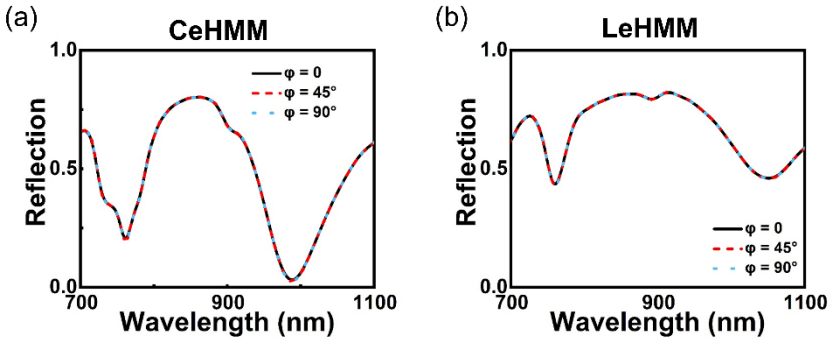

Fig. S10. For the (a) CeHMMs and (b) LeHMMs, their reflection spectra under elliptically polarized light with phase difference φ = 0°, 45° and 90°. Both structures exhibit polarization-independent properties with respect to φ.

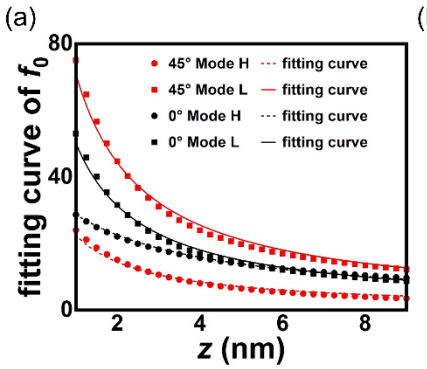

(b) Hyperbolic Fitting : $y = \frac{P_1 x}{P_2 + x}$

	P_1	P_2 ($\times 10^{-7}$)
45° Mode H	0.26	-1.49
45° Mode L	0.77	-1.49
0° Mode H	0.68	-1.47
0° Mode L	0.55	-1.49

Fig. S11. The hyperbolic fitting curve of f_0. (a) The fitting curve for the decay variation of EF enhancements in Mode H and Mode L across the range of z = 1-9 nm, excited by LPL with different polarization angle (θ): θ = 45° (red) and θ = 0° (black), solid and dashed lines represent the calculated values and fitted values of f_0, respectively. (b) Parameters derived from the hyperbolic fitting of all curves.

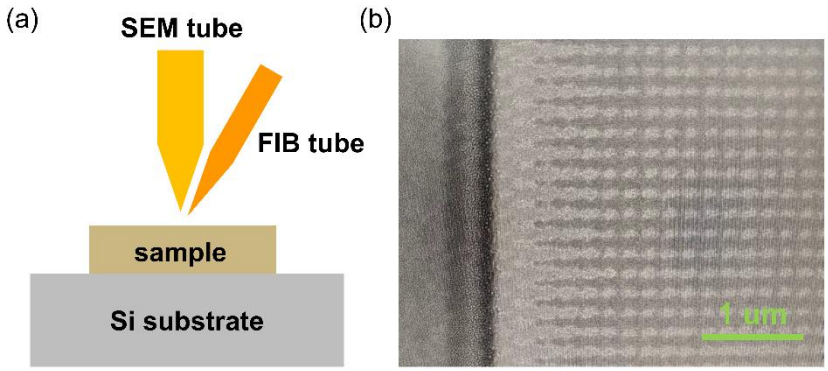

Fig. S12. Focused Ion Beam (FIB) technology. (a) Schematic diagram of FIB. (b) SEM image of the test sample etched by FIB technology. The precision of FIB-etched samples does not satisfy our required standards, whereas the EBL-etched samples (Fig. 5b-II) can demonstrate fabrication errors obviously smaller.

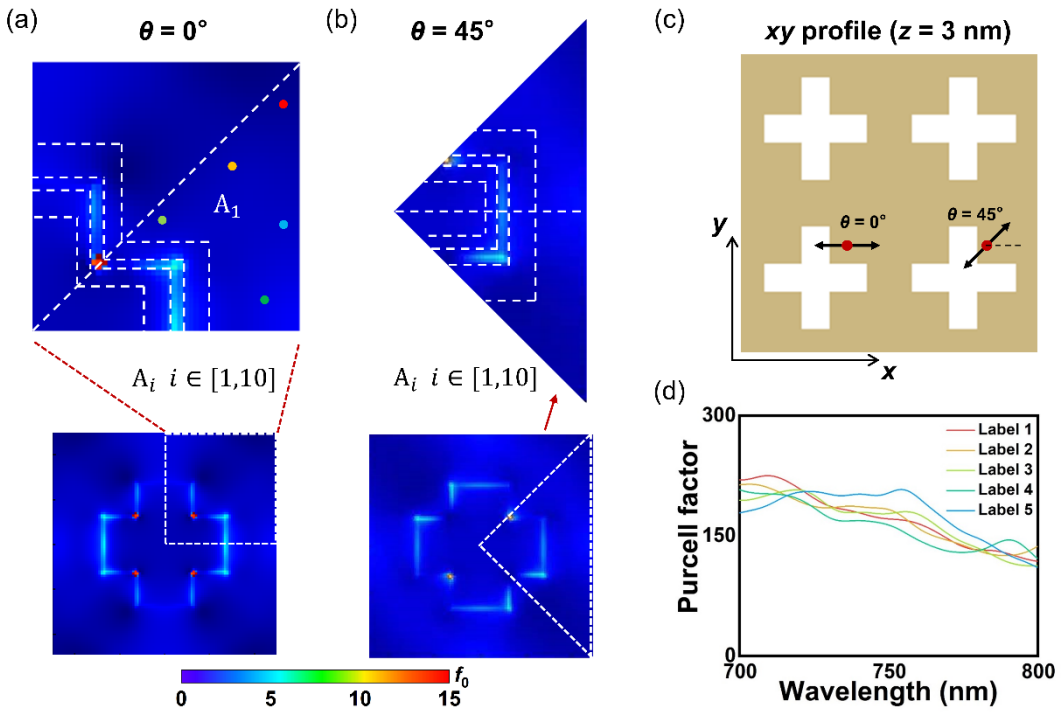

Fig. S13. Approximation and calculation of the average Purcell factor (P_f). At (a) θ = 0°and (b) θ = 45° LPL incidence, the surface EF enhancement distributions of the CeHMMs. (c) The polarization directions of the dipole sources. (d) Random sampling in region A_1 (colored points 1-5) generates the P_f curves in the wavelength range from 700 to 800 nm.

To estimate the PL enhancement of hotspot (F_{hs}) from the experimentally measured average (F_{ave}), the incident light must be considered when calculating the Purcell factor. Due to potential rotational misalignment of the WS_2/CeHMMs sample, different LPL need to be simulated. Fortunately, according to the structural symmetry, the EF enhancement distribution varies only between polarization angle θ = 0° and 45°, and f_0 changes within a narrow range (0 to 15, see Fig. S13a and Fig. S13b). Thus, the Purcell factors for θ = 0° and 45° are averaged to approximate the average Purcell factor (P_{ave}) of CeHMMs,

$$P_{ave} = \frac{P_{ave-0°} + P_{ave-45°}}{2} \quad \text{(S1)}$$

The Purcell factor was achieved by positioning a dipole at spatial spot and then simulating a transmission box region of 4 nm × 4 nm × 4 nm. Additionally, for linear incident light at θ = 0°, the polarization direction of dipole must be aligned with the x axis. And the θ = 45° needs to form an

angle of 45° with the *x*-axis.

Next, the calculations of $P_{\text{ave-0°}}$ and $P_{\text{ave-45°}}$ are divided into five steps. First, due to the characteristics of the EF enhancement distributions, only one-quarter of the regions in Fig. S13a and S13b are analyzed. Second, these quarter are divided into ten subregions (A_i, i = 1, 2, …, 10) based on the decay of the EF enhancement (Fig. S13a and S13b). Third, Purcell factors are calculated at selected spatial points (z = 3 nm) within each A_i subregion, and their average value approximates average Purcell factor $P_{\text{ave-Ai}}$ of A_i subregion, as follows:

$$P_{\text{ave-Ai}} = \sum_{m=1}^{n} \frac{P_{\text{ave-m}}}{n} \tag{S2}$$

where n denotes the number of spatial points, and $P_{\text{ave-m}}$ is the Purcell factor at point m. It is note that the choice of n is determined by the decay of the EF enhancement. Taking subregion A_1 (n = 46) as an example (Fig. S13a), five random points were selected for Purcell factor calculations, revealing minimal variation (160-200) within the wavelength range from 750 to 770 nm (Fig. S13c). This result validates the above calculated method of $P_{\text{ave-Ai}}$, enabling estimations from a limited number of spatial points.

Fourth, since both $\theta = 0°$ and $\theta = 45°$ are divided into ten subregions, we take $\theta = 0°$ as an example to obtain its $P_{\text{ave-0°}}$:

$$P_{\text{ave-0°}} = \sum_{i=1}^{10} \sigma_i \cdot P_{\text{ave-Ai}} \tag{S3}$$

where $P_{\text{ave-Ai}}$ denotes the average Purcell factor for the A_i subregion, i = 1, 2, …, 10, and σ_i represents the normalized area of the A_i subregion, defined as:

$$\sigma_i = \frac{S_i}{S_{\text{total}}} = \frac{S_i}{\sum_{i=1}^{10} S_i} \tag{S4}$$

Finally, based on above method, the calculated values of $P_{\text{ave-0°}}$ and $P_{\text{ave-45°}}$ are 148 and 176 at λ = 764 nm, respectively. Substituting these results into eq. S1 yields an approximate average Purcell factor of P_{ave} = 162 for CeHMMs.

Similarly, in the main text, P_{hs} at hot spots is derived from the following equation:

$$P_{hs} = \frac{P_{hs-0°} + P_{hs-45°}}{2} = 1036 \tag{S5}$$